Nowacka, AE.; Vismara, R.; Mercuri, G.; Moroni, M.; Palomino Roca, M.; Domasevitch, K.; Di Nicola, C.... (2020). Cobalt(II) Bipyrazolate Metal-Organic Frameworks as Heterogeneous Catalysts in Cumene Aerobic Oxidation: A Tag-Dependent Selectivity. Inorganic Chemistry. 59(12):8161-8172. https://doi.org/10.1021/acs.inorgchem.0c00481

Cobalt(II) bipyrazolate metal-organic frameworks as heterogeneous catalysts in cumene aerobic oxidation: a tag-dependent selectivity

Anna Nowacka,[a] *Rebecca Vismara,*[b] *Giorgio Mercuri,*[c] *Marco Moroni,*[b] *Miguel Palomino,*[a]

Kostiantyn V. Domasevitch,[d] *Corrado Di Nicola,*[e] *Claudio Pettinari,* [c,f] *Giuliano Giambastiani,*[c,g,h,i]

Francesc X. Llabrés i Xamena,[a,*] *Simona Galli,*[b,h,*] *Andrea Rossin* [c,h,*]

[a] Instituto de Tecnología Química, Universitat Politècnica de València, Consejo Superior de Investigaciones Científicas, Avda. de los Naranjos, s/n, 46022 Valencia, Spain.

[b] Dipartimento di Scienza e Alta Tecnologia, Università dell'Insubria, Via Valleggio 11, 22100 Como, Italy.

[c] Istituto di Chimica dei Composti Organometallici (ICCOM-CNR), Via Madonna del Piano 10, 50019 Sesto Fiorentino, Italy.

[d] Taras Shevchenko National University of Kyiv, Volodymyrska Str. 64/13, 01601 Kyiv, Ukraine.

[e] Scuola di Scienze e Tecnologie, Università di Camerino, Via S. Agostino 1, 62032 Camerino, Italy

[f] Scuola del Farmaco e dei Prodotti della Salute, Università di Camerino, Via S. Agostino 1, 62032 Camerino, Italy.

[g] Institute of Chemistry and Processes for Energy, Environment and Health (ICPEES), UMR 7515 CNRS-University of Strasbourg (UdS), 25, rue Becquerel, 67087 Strasbourg Cedex 02, France.

[h] Consorzio Interuniversitario Nazionale per la Scienza e Tecnologia dei Materiali, Via Giusti 9, 50121 Firenze, Italy.

[i] Kazan Federal University, Alexander Butlerov Institute of Chemistry, 420008 Kazan, Russian Federation.

Authors to whom correspondence should be addressed: fllabres@itq.upv.es; simona.galli@uninsubria.it; a.rossin@iccom.cnr.it.

KEYWORDS. – Advanced porous materials - Metal-Organic Frameworks (MOFs) – cobalt(II) – nitrogen-based ligands – dioxygen adsorption – heterogeneous oxidation catalysis

ABSTRACT. Three metal-organic frameworks with general formula **Co(BPZX)** ($BPZX^{2-}$ = 3-X-4,4'-bipyrazolate, X = H, NH_2, NO_2) constructed with ligands having different functional groups on the same skeleton have been employed as heterogeneous catalysts for aerobic liquid-phase oxidation of cumene with O_2 as oxidant. O_2 adsorption isotherms collected at p_{O2} = 1 atm and T = 195 and 273 K have cast light on their relative affinity for dioxygen. The highest gas uptake at 195 K is found for **Co(BPZ)** [3.2 mmol/g (10.1 wt. % O_2)], in line with its highest BET specific surface area (926 m^2/g) if compared with those of **Co(BPZNH$_2$)** (317 m^2/g) and **Co(BPZNO$_2$)** (645 m^2/g). The O_2 isosteric heat of adsorption (Q_{st}) trend follows the order **Co(BPZ) > Co(BPZNH$_2$) > Co(BPZNO$_2$)**. Interestingly, the selectivity in the cumene oxidation products was found to be dependent on the tag present in the catalyst linker: while cumene hydroperoxide (CHP) is the main product obtained with **Co(BPZ)** (84% selectivity to CHP after 7 h, p_{O2} = 4 bar and T = 363 K), further oxidation to 2-phenyl-2-propanol (PP) is observed in the presence of **Co(BPZNH$_2$)** as the catalyst (69% selectivity to PP under the same experimental conditions).

1. INTRODUCTION

Oxidation of Cumene (CM) to cumene hydroperoxide (CHP) is an interesting process from the industrial viewpoint, as CHP is an intermediate for the synthesis of phenol, an important raw material for phenol resins, perfumes, medicines, agricultural chemicals and many other industrial products with added-value.[1] CM oxidation (Scheme 1) is typically carried out in the liquid phase, using O_2 (or air) as oxidant in the absence of any catalyst (the so-called thermal auto-oxidation process) and with small amounts of CHP or other substances added as initiators. CM conversion is usually kept low to maximize the selectivity towards CHP (typically above 90–92%) and minimize side products resulting from CHP decomposition, mainly 2-phenyl-2-propanol (cumyl alcohol, PP) and acetophenone (AP) (Scheme 1, paths a and b).[2] Despite these precautions, the productivity of the auto-oxidation process is generally below the desired values.

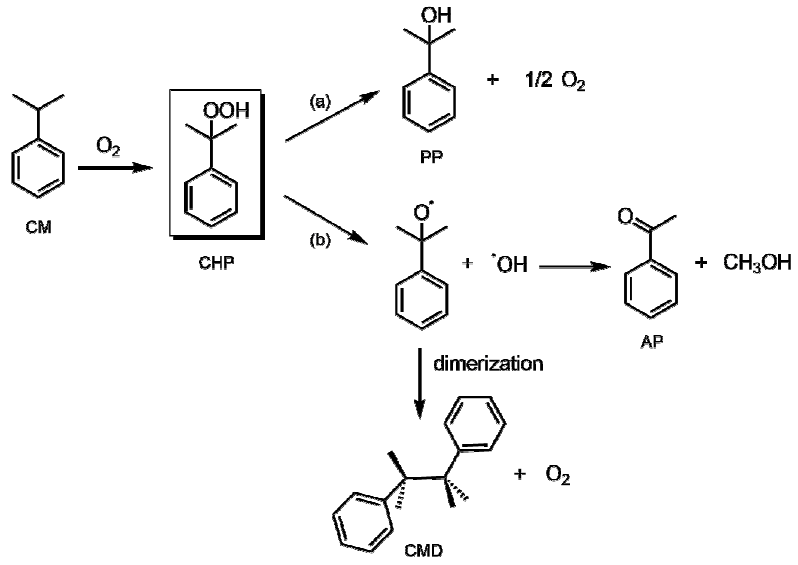

Scheme 1. Schematic representation of CM oxidation to CHP and its further oxidation to yield 2-phenyl-2-propanol (PP, a) and acetophenone (AP, b).

To solve this problem, there is a large interest in developing robust and re-usable homogeneous and heterogeneous catalysts for CM oxidation to increase CHP productivity without compromising the high selectivity typically attained in the auto-oxidation process.[3] Most of these catalysts are based

on transition metals, which are active in several catalytic oxidation reactions. For example, Zhang *et al.*[4] used CuO nanoparticles as catalyst and O_2 as oxidant at 358 K, attaining a very good selectivity to CHP (93.2%) at a relatively high conversion level (44.2%). This catalyst could be reused up to six times without activity loss. Hsu *et al.*[5] studied various polymer-supported transition metal catalysts for CM oxidation at 353 K in O_2 atmosphere. The best results achieved featured a 99% selectivity at a 6.8% conversion, with a reaction rate that was 84% faster than blank experiment (auto-initiated with CHP) under analogous conditions. Nonetheless, the most widely exploited transition metal in CM oxidation catalysis is cobalt. Several literature examples featuring both homogeneous and heterogeneous cobalt-based systems can be found. As a representative example, the $[Co(N_3Py_2)(H_2O)](ClO_4)_2$ and $[Co(N_3Py_2)(CH_3CN)](BPh_4)_2$ complexes (N_3Py_2 = κ^5-*N*-pentadentate pyridine-based ligand) reported in 2017[6] belong to the former class. The latter family is definitely bigger, spanning from Co-salen-polymers,[7] a $Co(OAc)_2/SiO_2$ xerogel composite[8] and simple CoX_2 salts (X^- = Cl^-, OAc^-, $acac^-$)[9] to the mixed-valence spinel Co_3O_4 [10] and modified cobalt oxides.[11]

Besides the production of CHP commented above, CM oxidation is important for other applications as well. Indeed, many catalysts that are highly active for CM oxidation are also very active in converting CHP into its two main byproducts: PP and AP. Like phenol, also PP and AP are valuable intermediates in the production of resins, perfumes or pharmaceuticals.[12] It is therefore interesting to learn how the properties of a catalyst can be tuned to promote either the selective formation of CHP, or its further decomposition to the target products PP and AP, while avoiding accumulation of CHP in the reaction mixture to reduce safety concerns.

Among the plethora of heterogeneous catalysts available, in recent years Metal-Organic Frameworks (MOFs) have gained the stage as versatile and multi-functional catalysts in several chemical processes.[13] MOFs are crystalline and porous materials, and their chemico-physical properties can be easily tuned through a judicious combination of tailored organic linkers and metallic nodes. Thus, MOFs are superior heterogeneous catalysts if compared to the "classical" fully inorganic zeolites/oxides or to fully organic carbon-based nanomaterials. In the specific context of alkanes and

alkenes oxidation catalysis, several transition metal-based MOFs have been scrutinized by different research groups Worldwide.[14] Similarly to what observed with other heterogeneous catalysts, the most exploited transition metal for MOFs construction in this applicative context is cobalt.[15]

In previous investigations, we have shown that MOFs containing transition metals of the *3d* series like Cu(2-pymo)$_2$,[16] Cu(im)$_2$,[16] Cr,Fe-MIL-101[17] and the mixed-metal NiCo-BTC series[18] can be employed as catalysts for the aerobic oxidation of alkanes, including cumene. In light of this, and starting from our expertise in the preparation of transition-metal-containing bipyrazolate MOFs with ligands decorated with different chemical tags,[19] we have isolated the new cobalt(II) MOF **Co(BPZNH$_2$)** containing the 3-amino-4,4'-bipyrazole spacer (H_2BPZNH_2, Scheme 2) and we have tested it as heterogeneous catalyst in cumene oxidation under mild conditions using oxygen as green oxidant (T = 363 K, p_{O2} = 4 atm), together with the already known analogues **Co(BPZ)** (H_2BPZ = 4,4'-bipyrazole, Scheme 2) and **Co(BPZNO$_2$)** (H_2BPZNO_2 = 3-nitro-4,4'-bipyrazole, Scheme 2), sharing the same structural motif. Different selectivity has been observed, as a function of the nature of the chemical tag present in the catalyst ligand. The selectivity trend found is strongly connected with the ability of the scrutinized MOFs to promote further CHP oxidation.

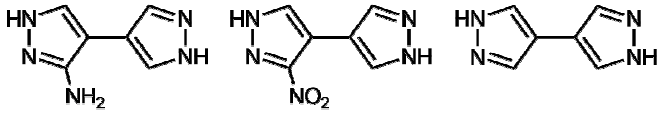

Scheme 2. Molecular structure of the three spacers employed in this work: 3-amino-4,4'-bipyrazole (H_2BPZNH_2, left), 3-nitro-4,4'-bipyrazole (H_2BPZNO_2, centre) and 4,4'-bipyrazole (H_2BPZ, right).

2. EXPERIMENTALS

2.1. Materials and Methods

All the reagents and solvents used were acquired from commercial vendors and employed as received, without purification. 4,4'-Bipyrazole,[20] 3-nitro-4,4'-bipyrazole,[21] 3-amino-4,4'-

bipyrazole,[19b] **Co(BPZ)**[19e] and **Co(BPZNO$_2$)**[19c] were prepared following previously published procedures. Elemental analyses (C, H, N %) were carried out on a Fisons Instruments 1108 CHNS-O elemental analyser. IR spectra were recorded as neat from 4000 to 600 cm^{-1} using a PerkinElmer Spectrum One System instrument. Thermogravimetric analysis (TGA) and differential scanning calorimetry (DSC) were simultaneously carried out using a NETZSCH STA 409 PC analyser on the **Co(BPZNH$_2$)·DMF** and the activated **Co(BPZNH$_2$)** compounds. As for the former, ~10 mg of as-synthesised **Co(BPZNH$_2$)·DMF** were heated in an oven at 323 K for 4 hours; then, they were placed in an alumina crucible devoted to the thermal analysis. As for the latter, ~10 mg of as-synthesised **Co(BPZNH$_2$)·DMF** were activated at 413 K under vacuum (10^{-3} bar) for 24 h; then, they were placed in an alumina crucible. Under a N_2 flow (40 mL min^{-1}), the temperature was increased from 303 to 1173 K or 1073 K with a rate of 10 K min^{-1}. The raw data obtained were corrected on the basis of a background curve. The nature and purity of all the samples used in this work were evaluated by elemental analysis, IR spectroscopy and powder X-ray diffraction (PXRD). PXRD qualitative analyses were performed by means of a Bruker AXS D8 Advance vertical-scan θ:θ diffractometer equipped with an X-ray tube (CuKα, λ = 1.5418 Å), a Bruker Lynxeye linear position-sensitive detector, a filter of nickel in the diffracted beam, and the following optical components: primary beam Soller slits (2.5°), fixed divergence slit (0.5°), antiscatter slit (8 mm). The generator was operating at 40 kV and 40 mA. PXRD data were measured at room temperature conditions in the 2θ range 5.0–105.0°, with steps of 0.02° and a time per step of 10 s, and treated with whole powder pattern refinements, with the algorithms of the TOPAS-Academic V6 software package.[22] XPS spectra were recorded using a SPECS spectrometer equipped with a Mg Kα (1253.6 eV) X-ray source and a 150MCD-9 Phoibos detector. The spectra were corrected using the sp^2 graphitic component of the C 1s spectrum as internal reference (binding energy, BE, 284.6 eV). Morphology of the samples was analyzed with a Field Emission Scanning Electron Microscope (FESEM) model JEOL JSM-7001F.

2.2. Synthesis of Co(BPZNH$_2$)·DMF

$Co(NO_3)_2 \cdot 6H_2O$ (0.291 g, 1.00 mmol) was added to a *N*,*N*-dimethylformamide (DMF) solution (15 mL) of 3-amino-4,4'-bipyrazole (0.149 g, 1.00 mmol). The mixture was stirred at 393 K for 24 h. After slow cooling to room temperature, a dark violet precipitate was formed. The precipitate was filtered off, washed with hot DMF (2×10 mL) and dried under vacuum. Yield: 73%. **Co(BPZNH$_2$)·DMF** is insoluble in dimethyl sulfoxide, alcohols, acetone, acetonitrile, chlorinated solvents and water. Elem. Anal. Calc. for $Co(BPZNH_2) \cdot 0.75(DMF)$: C, 37.98; H, 3.96; N, 30.87%. Found: C, 37.94; H, 3.94; N, 30.79%. IR (neat, cm^{-1}; Figure S1): 3387 (w,br) [ν(N–H)], 3095 (w) [$\nu(C–H_{aromatic})$], 2928 (w) [$\nu(C–H_{aliphatic})$], 1655 (vs) [ν(C=O)], 1500 (s) [ν(C=C+C=N)], 1435 (w), 1384 (s), 1275 (m), 1250 (m), 1204 (w), 1163 (w), 1123 (s), 1093 (m), 1056 (s), 1014 (w), 946 (s), 839 (m).

2.3. Powder X-ray Diffraction Structural Characterization

Samples of **Co(BPZNH$_2$)·DMF** or **Co(BPZNH$_2$)** were placed in the cavity of a silicon free-background sample-holder 0.2 mm deep (Assing Srl, Monterotondo, Italy). PXRD data acquisitions were carried out with the instrumentation described above in the 2θ range 5.0-105.0°, with steps of 0.02° and an overall scan time of about 12 hours. Though retraceable to those of other M(bipyrazolate) MOFs (M = Co, Zn)[19b, 19c, 19e] with orthorhombic *Cccm* crystallographic symmetry, the PXRD patterns of all the as-synthesized samples of **Co(BPZNH$_2$)·DMF** we handled showed doubling or right-side anisotropic broadening of specific Miller indexes classes (e.g. [*hhl*], [0*kl*] and [*h*0*l*]), with respect to the PXRD pattern calculated based on the supposed orthorhombic *C* crystallographic symmetry. This is also witnessed by a whole powder pattern refinement performed with the Le Bail method, with the algorithms of the TOPAS-Academic V6 software package (Figure S2). Lowering the crystallographic symmetry (*e.g.* down to *C*2/*c* or $P2_1/c$, proper subgroups of *Cccm*) did not lead to any improvement. Similarly, *ab initio*

indexing (*i.e.* peak search followed by profile fitting to estimate the maximum positions of low-to-medium-angle peaks, which were then handled through the Singular Value Decomposition algorithm[23] within TOPAS-Academic V6) did not lead to trustable unit cells describing all the observed reflections. On the contrary, the powder pattern could be successfully modeled *via* a whole powder pattern refinement by using two *Cccm* unit cells with slightly different parameters (Figure S3, Table S1). The difference in the asymmetric unit volume (~4 $Å^3$, estimated as *V*/*Z*'; Table S1) cannot be explained in terms of two phases with a different solvation degree. Indeed, *ex situ* activation (T = 413 K, 10^{-3} Torr, 24 h) or *in situ* heating of an as-synthesized sample at a temperature above that needed for complete solvent removal (see the section devoted to the thermal behavior) did not provide a unique phase. Upon activation, the two powder patterns coalesce into one that can be described only apparently by the unit cell parameters of one orthorhombic *C* phase (Figure S4). Despite the adoption of various models with different complexity to describe the peak profile [*e.g.* convolution, to a Lorentian description, of *hkl*-class specific tan(θ)- or 1/cos(θ)-dependent spherical harmonics], some Bragg reflections are still right-side anisotropically broadened. The issue could be fixed by assuming that the sample is biphasic even after activation (Figure S5). On the basis of recent seminal works on conditioned disorder in MOFs,[24] we propose that this experimental evidence can be explained by the existence of two phases in which the ligands locally adopt different conditioned order of the NH_2 substituents. In the hypothesis that the bipyrazolate ligand is not planar (an occurrence already observed in the literature even with unsubstituted bipyrazolates[19e, 20, 25]) we can think of three mutual dispositions of the NH_2 groups (Figure 1) along the *a*- and *b*-axis.

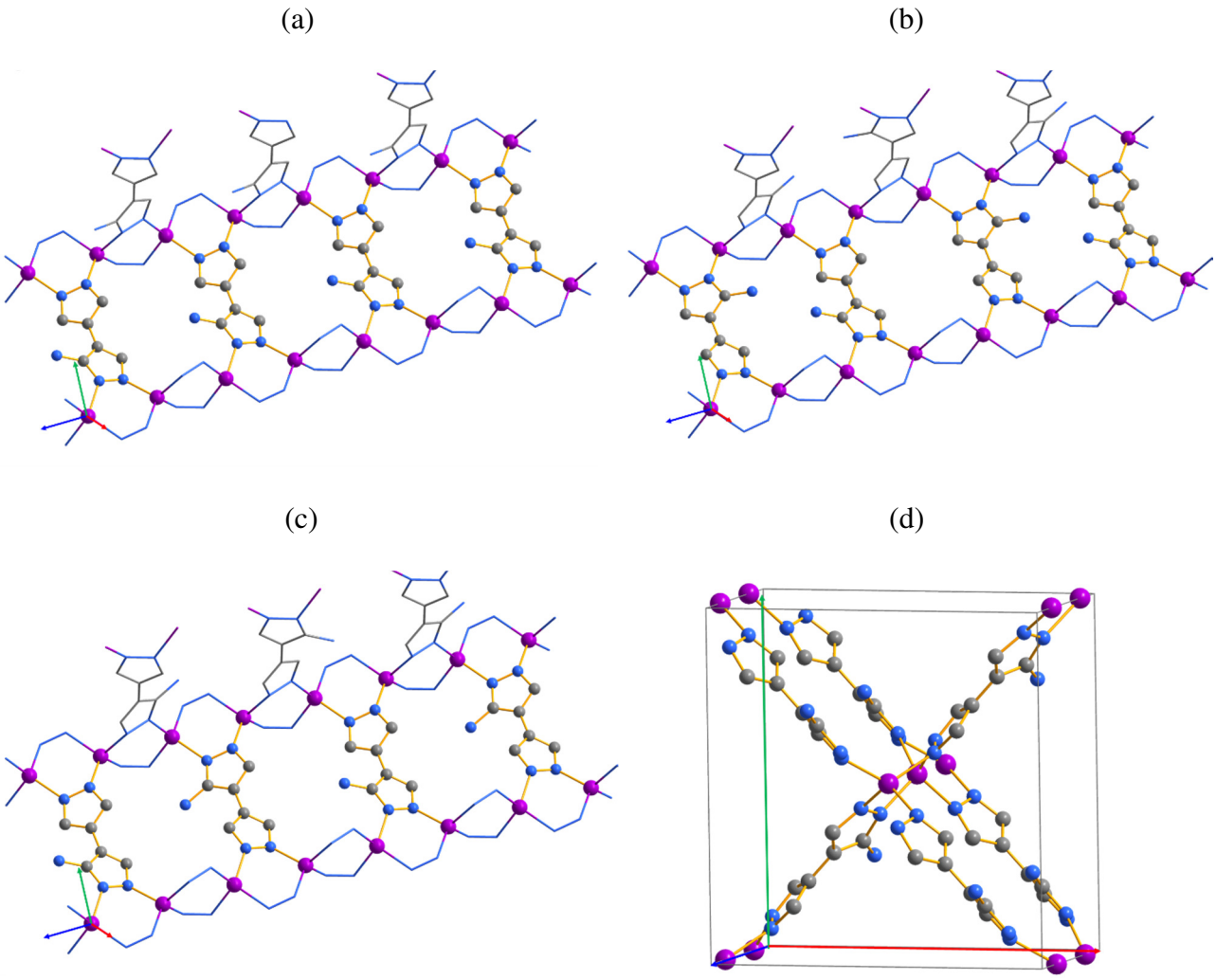

Figure 1. Conditioned order in **Co(BPZNH$_2$)**: (a)-(c) possible mutual dispositions of the amino groups along the pore walls, assuming that the 3-amino-4,4'-bipyrazolate ligand is not planar. (d) Portion of the packing as reference. Axis color code: *a*, red; *b*, green; *c*, blue. Atom color code: carbon, grey; nitrogen, blue; zinc, violet. The hydrogen atoms have been omitted for clarity.

Thus, phases featured by slightly different unit cell parameters can be obtained, depending on the conditioned order adopted by the -NH$_2$ dangling groups. Heating promotes a disruption of this order until the two phases coalesce almost completely. As a proof of evidence, a structure refinement was carried out through the Rietveld method using two orthorhombic *Cccm* phases, starting from the

crystal structure of Zn(BPZNO$_2$).[19c] A rigid body was built up to model the crystallographically independent portion of the ligand, assigning mean values to bond distances and angles,[26] and without constraining the two pyrazolate rings to be coplanar. The amino group was maintained co-planar to the skeleton of the ligand. Even though for the final structure refinement **Co(BPZNH$_2$)** was preventively activated (413 K, 10^{-3} bar, 24 h) to eliminate the guest solvent, the MOF adsorbs water vapour from the atmosphere simply during its transfer from the vacuum apparatus to the alumina crucible for the thermogravimetric analysis. This is witnessed by a thermal analysis performed on the activated sample (Figure S6). To locate the adsorbed water molecules, structure solution was carried out with TOPAS-Academic V6 by a combined Monte Carlo/Simulated Annealing[27] approach using a number of oxygen atoms whose site occupation factors and fractional coordinates were let vary. During the final stages of the Rietveld refinement, ligand bond distances (except the C/N-H distances) were refined in a restrained range of values, based on a search in the Cambridge Structural Database (v. 2019) for room-temperature crystal structures containing the M(pyrazolate) (M = *3d* transition metal) fragment. The background was modelled through a Chebyshev-type polynomial function. A common, refined isotropic thermal factor (B_{iso}) was attributed to all atoms, except to the metal centre, whose isotropic thermal factor was calculated as $B_{iso}(M) = B_{iso} - 2.0$ (Å^2). The peak profile was modelled through the Fundamental Parameters Approach.[28] The anisotropic peak profile of the two phases was modelled by convoluting the same tan(θ) contribution of the Stephens correction.[29] The final Rietveld refinement plot is provided as Figure S7 of the Electronic Supplementary Information. The CIF file is supplied as Electronic Supplementary Information (the CIF file of **Phase 1** is provided as a representative example). The final m/m ratio (%) of the two phases found at the end of the refinement process is 66:34.

Crystal data for **Co(BPZNH$_2$)·2.5H$_2$O**, **Phase 1**: $C_6H_{10}CoN_5O_{2.5}$, FW = 251.1 g mol^{-1}, orthorhombic, *Cccm*, *a* = 12.350(7) Å, *b* = 12.815(8) Å, *c* = 7.2225(14) Å, V = 1143.1(10)

Å^3, Z = 16, Z' = 4, ρ = 1.460 g cm^{-3}, F(000) = 512, R_p = 0.014, R_{wp} = 0.018, R_{Bragg} = 0.006, for 4826 data and 44 parameters in the 2θ range 8.5-105.0°. CCDC Number: 1962311.

Crystal data for **Co(BPZNH$_2$)·0.8H$_2$O**, **Phase 2**: $C_6H_{6.6}CoN_5O_{0.8}$, FW = 220.5 g mol^{-1}, orthorhombic, *Cccm*, a = 12.530(12) Å, b = 12.758(13) Å, c = 7.2400(11) Å, V = 1157.4(16) Å^3, Z = 16, Z' = 4, ρ = 1.265 g cm^{-3}, F(000) = 444, R_p = 0.014, R_{wp} = 0.018, R_{Bragg} = 0.007, for 4826 data and 44 parameters in the 2θ range 8.5-105.0°.

2.4. Variable-Temperature Powder X-ray Diffraction

In order to complete the thermal analysis, the thermal behaviour of **Co(BPZNH$_2$)·DMF** was studied *in situ* by means of variable-temperature PXRD. A sample of ~20 mg of as-synthesized **Co(BPZNH$_2$)·DMF** was heated in air from 303 K up to 623 K employing a custom-made sample heater (Officina Elettrotecnica di Tenno, Ponte Arche, Italy), with steps of 20 K; a PXRD pattern was measured at all steps in the 2θ range 9.0-24.5°, with a step of 0.02° and a time per step of 1.5 s.

2.5. Gas Adsorption

~40 mg samples of the three MOFs were activated at 403 K under high vacuum (10^{-6} Torr) for 24 h prior to every measurement. The textural properties of **Co(BPZNH$_2$)** were estimated by volumetric adsorption carried out with an ASAP 2020 Micromeritics instrument, using N_2 as adsorbate at 77 K. For the Brunauer–Emmett–Teller (BET) specific surface area calculation, the 0.01-0.1 p/p^0 pressure range of the isotherm was used for data fitting to satisfy all the Rouquerol's consistency criteria.[30] The pore size distribution was determined by means of the BJH method (Halsey thickness equation) for the mesopores, and with the density functional theory method (DFT - slit-like pore shape typical of carbon-based materials) for the micropores. The micropore volume was estimated by applying the Dubinin-Astakhov model to the N_2 adsorption isotherm in the pressure range $0 \leq p/p^0 \leq 0.02$.[31] The O_2 isosteric

heat of adsorption (Q_{st}) of the **Co(BPZX)** MOFs was calculated from the O_2 isotherms measured at 273 and 195 K by applying a variant of the Clausius-Clapeyron equation:[32]

$$\ln\left(\frac{p_1}{p_2}\right) = Q_{st} \times \frac{T_2 - T_1}{R \times T_1 \times T_2} \qquad \text{(Equation 1)}$$

where p_n (n = 1 or 2) is the pressure value for the n^{th} isotherm; T_n (n = 1 or 2) is the temperature value for the n^{th} isotherm; R is the gas constant (8.314 J K^{-1} mol^{-1}).

2.6. Oxidation of cumene

CAUTION!! The reaction conditions of cumene oxidation have been carefully selected to avoid flammable mixtures. Any deviation from these conditions must be carefully evaluated. In a typical experiment, 1 mL of cumene (7.14 mmol, 99%, Sigma-Aldrich) and the solid catalyst [**Co(BPZ)**, **Co(BPZNO$_2$)** or **Co(BPZNH$_2$)**, with a cumene-to-metal molar ratio = 150] were placed inside a glass tube microreactor (volume = 6 mL) with a magnetic stirrer, a manometer, a gas inlet and a valve for liquid sampling. The reactor was connected through a cannula to an O_2 supply system fixed at p_{O2} = 4 bar. The reservoir continuously restock the O_2 consumed during the oxidation reaction, to keep the concentration of O_2 constant during the reaction. The reactor was placed on an iron hot plate pre-heated at 363 K. To monitor the time evolution of the products we used GC analysis (Agilent Technologies 7890A, capillary column 10 m × 320 μm × 0.1 μm) on aliquots taken at fixed time intervals. To minimize the possible decomposition of the hydroperoxide at the injector, the samples were injected directly on-column. The metal content of the reaction filtrate was determined by ICP-OES on a Varian 715-ES instrument.

2.7. Cumene Hydroperoxide Decomposition

For CHP decomposition experiments, the same glass tube microreactors were used, containing 1 mL of cumene (7.14 mmol), 14 mg of catalyst [**Co(BPZ)**, **Co(BPZNO$_2$)** or **Co(BPZNH$_2$)**] and

diphenylether as internal standard (50 μL). After flushing the reactor with N_2, CHP was added (110 μL) and the reaction vessel was placed in an iron heating block at 363 K. The conversion of CHP was determined by GC.

2.8. Heat of Immersion Experiments

A precise weighted mass of catalyst was placed in a glass bulb with a brittle end, and outgassed under high vacuum (10^{-5} mbar) for 24 h at 333 K. The bulb was then sealed and transferred to a Setaram Calvet-type C80 calorimeter equipped with a mixing cell containing 4.00 g of the wetting liquid (either CM or CHP) and tightly sealed by an O-ring. The system was placed into the calorimeter block and left for temperature equilibration (303 K). When thermal equilibrium was reached, the cell rod was gently pressed to break the brittle end of the bulb with the bottom of the calorimeter cell. The wetting liquid entered into the sample, and the evolution of the released heat was monitored as a function of time. Total experimental heat of immersion was then calculated by integrating this signal, after correcting by measuring empty (reference) cells under the same conditions to account for bulb breaking (exothermic event), and heat of vaporization of the wetting liquid filling the empty volume of the bulb with the vapor at the corresponding vapor pressure (endothermic event).

3. RESULTS AND DISCUSSION

3.1. Synthesis of Co(BPZNH$_2$)·DMF and Crystal Structure Analysis

The synthesis of **Co(BPZNH$_2$)·DMF** does not require the application of solvothermal conditions. In this case, the conventional synthetic path is equally viable using *N,N*-dimethylformamide as solvent. Moreover, ligand deprotonation does not require the presence of a base. The MOF precipitates out of the reaction mixture as a dark violet air-stable powder insoluble in the most common organic solvents. **Co(BPZNH$_2$)** shows the same structural motif of **Co(BPZ)**[19e] and **Co(BPZNO$_2$)**.[19c] A short description of the key structural aspects is provided hereafter for the sake

of completeness. **Co(BPZNH$_2$)** crystallizes in the orthorhombic space group *Cccm*. As explained in the Experimental Section, in all the examined batches of **Co(BPZNH$_2$)** two phases are present with slightly different unit cell parameters and ligand conformation. Indeed, the intrinsic asymmetry of the ligand may create a locally different conditioned order of the amino substituents (Figure 1). In **Co(BPZNH$_2$) Phase 1** a torsion angle of ~20° is present between the two pyrazolate rings, while **Co(BPZNH$_2$) Phase 2** contains a planar ligand (Figure 2a). In the crystal structure of **Co(BPZNH$_2$)**, tetrahedral CoN_4 nodes and *exo*-tetradentate spacers build up a 3-D (4,4)-connected open framework (Figure 2b), featuring 1-D channels of rhombic shape parallel to the crystallographic direction [001]. The channels aperture (distance between the Van der Waals sphere of the closest carbon atoms belonging to parallel facing ligands = 5.0 and 5.5 Å for **Phases 1** and **2**, respectively) and consequently the accessible volume, are strictly dependent on the orientation of the ligand and the torsion angle between its pyrazolate rings. At room temperature and pressure conditions, the empty volume[33] of the two phases lays in the range 44-46%, which means a pore volume of ~0.37-0.39 cm^3 g^{-1}. The **sra** network type is unveiled by the topological analysis carried out with TOPOS 4.0.[34]

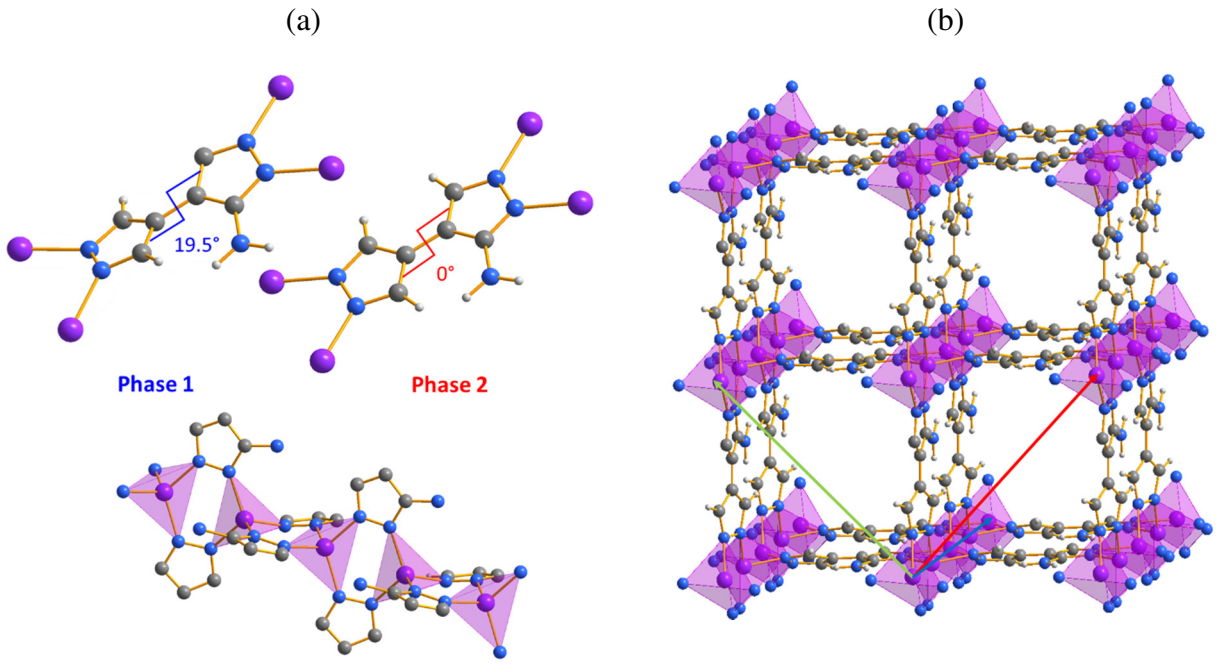

Figure 2. Representation of the crystal structure of **Co(BPZNH$_2$)**: (a) the torsion angles between the two ligand pyrazolate rings in **Phase 1** and **Phase 2** and their coordination mode through the 1-D chains along the [001] crystallographic direction. (b) Portion of the packing of **Co(BPZNH$_2$) Phase 1** viewed in perspective along the [001] crystallographic direction. Carbon, grey; hydrogen, light grey; cobalt, violet; nitrogen, blue. For the sake of clarity, the solvent molecules have been omitted and an ordered model has been assumed for the position of the NH_2 groups on the skeleton of the ligand, by lowering the symmetry down to *C*2. Main bond distances and angles: **Phase 1**: Co-N, 2.062(2), 2.081(2) Å; Co···Co, 3.611(2), 8.899(6) Å; N-Co-N, 109.6(6)-110.8(6)°; **Phase 2**: Co-N, 2.051(5) Å; Co···Co, 3.620(4), 8.941(6) Å; N-Co-N, 108(2)-112.7(14)°.

3.2. Thermal Behaviour

Before performing the simultaneous thermal analysis (STA), a batch of as-synthesized **Co(BPZNH$_2$)·DMF** was maintained in an oven at 323 K for 4 hours, to eliminate traces of humidity on the outer surface of the material. As shown by the TGA trace (Figure S8a), the MOF is stable under N_2 up to ~673 K (onset of the decomposition temperature), showing a better thermal

stability than **Co(BPZ)** (T_{dec} = 593 K)[19e] and **Co(BPZNO$_2$)** (T_{dec} = 623 K).[19c] Before decomposition, two weight losses take place (~2.9% in the temperature range 303-351 K; ~19.0% in the temperature range 370-583 K). The first one can be confidently attributed to the water vapour adsorbed by the sample during its transfer from the oven to the thermal analyser. The second one can be reasonably explained as the loss of 0.7 mol of DMF per mol of MOF (calculated weight loss 19.6%). *In situ* variable-temperature PXRD performed in air on a sample of **Co(BPZNH$_2$)·DMF** shows that the MOF is permanently porous (Figure S8). The two *Cccm* phases are clearly visible (in terms of peak doubling) up to 423 K (blue traces in Figure S8b); starting from 443 K, their PXRD patterns coalesce and right-side anisotropic broadening of specific classes of Miller indexes is evident (see the Experimental Section). At 623 K, crystallinity loss is complete.

3.3. N_2 Adsorption

The textural properties of **Co(BPZNH$_2$)** were investigated through N_2 adsorption at 77 K after thermal activation (403 K, 10^{-6} Torr, 24 h). As shown in Figure 3, **Co(BPZNH$_2$)** is featured by a type IV isotherm with a narrow hysteresis loop typical of a mainly microporous material with slit-like pore shape; the calculated BET specific surface area is 317 m^2/g (Table 1). This value is similar to that of Zn(BPZNH$_2$) (395 m^2/g),[19b] but lower than the **Co(BPZ)** (926 m^2/g)[19e] and **Co(BPZNO$_2$)** (645 m^2/g)[19c] analogues. The total pore volume at p/p^0 = 0.98 is 0.21 cm^3/g. The limiting micropore volume (0.14 cm^3/g) estimated through the Dubinin-Astakhov model to the N_2 adsorption isotherm is much lower than the pore volume calculated from the crystal structure (~0.38 cm^3/g, *vide supra*). This suggests that the real sample porosity is different from the crystallographic one obtained through purely geometrical considerations. Indeed, this structural motif[19b, 19c, 19e] has already shown a certain extent of framework flexibility that may vary the pore size. The Dubinin-Astakhov analysis also revealed that the micropore volume represents the main contribution to the total pore volume (67%). In **Co(BPZNH$_2$)** there are two different micropore sizes (retrieved from the DFT analysis – slit pore shape of carbon-based materials)

of 1.4 and 1.6 nm. The narrow and extended hysteresis loop for $p/p^0 > 0.42$ can be ascribed to interparticle voids between crystallites in the sample, as confirmed by the SEM analysis of a bulk sample of the MOF (*vide infra*, Section 3.5). The BJH analysis applied to the desorption branch of the N_2 isotherm did not find any mesopores in the 5-50 nm pore width interval; the only peak observed at $w \approx 3.9$ nm is an artefact due to cavitation of the liquid nitrogen meniscus at $p/p^0 = 0.42$.[35]

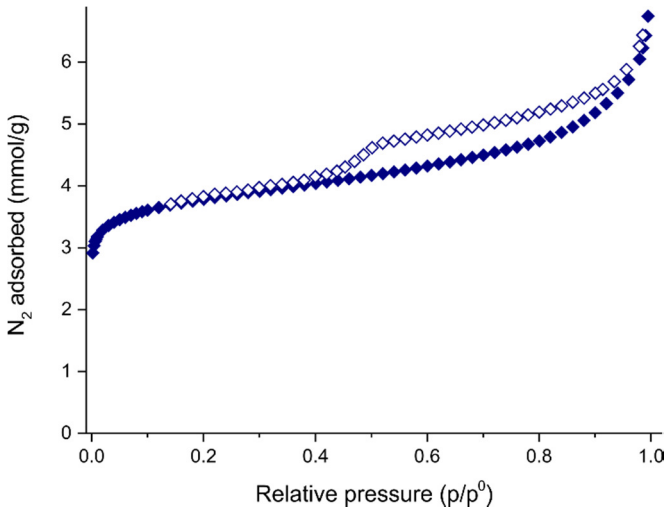

Figure 3. N_2 adsorption isotherm measured at 77 K on **Co(BPZNH$_2$)**. The desorption branch is drawn with empty symbols.

3.4. O_2 Adsorption

Given the use in catalysis of O_2 as green oxidant, the **Co(BPZX)** MOFs were tested as O_2 adsorbents at T = 195 and 273 K and p_{O2} up to 1 bar (Figure 4 and Figure S9, respectively). Table 1 collects the main O_2 adsorption data. **Co(BPZNO$_2$)** is the best O_2 adsorbent at high temperatures, while **Co(BPZ)** is the best O_2 adsorbent at low temperatures. In terms of weight percentage, the amount of O_2 adsorbed at 195 K is proportional to the respective BET areas.

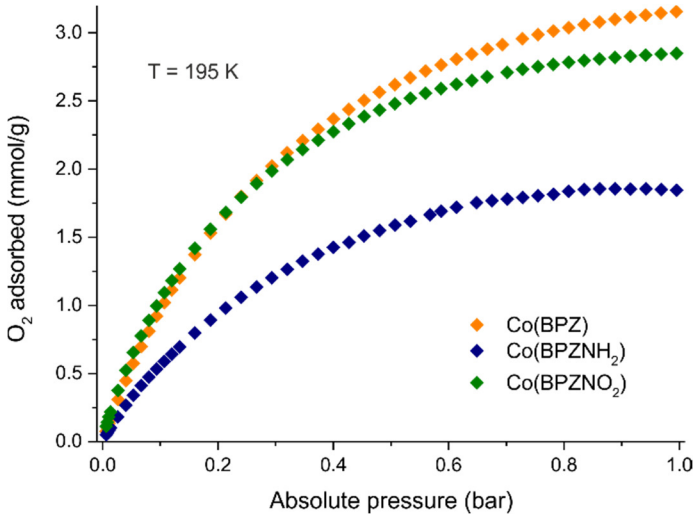

Figure 4. O_2 adsorption isotherms measured at 195 K on **Co(BPZX)**.

Table 1. Collective data on BET areas, as retrieved from the N_2 adsorption isotherm, O_2 uptake (at p = 1 bar; T = 273 K and 195 K) and oxygen isosteric heat of adsorption (Q_{st}) of the **Co(BPZX)** MOFs presented in this work.

	BET area (m^2/g)	O_2 adsorbed (mmol/g)		$Q_{st}(O_2)$
		273 K	195 K	(kJ/mol)
Co(BPZ)	926[19e]	0.6 (2.0 wt.%)	3.2 (10.1 wt.%)	17.7
Co(BPZNO$_2$)	645[19c]	1.1 (3.5 wt.%)	2.8 (9.1 wt.%)	13.7
Co(BPZNH$_2$)	317	0.5 (1.6 wt.%)	1.8 (5.9 wt.%)	15.9

The isosteric heat of adsorption (Q_{st}) of O_2 was estimated with a variant of the Clausius-Clapeyron equation (Equation 1, through the comparison of the O_2 adsorption isotherms recorded at 273 and 195 K). The results are shown in Table 1. The isosteric heat of adsorption reflects the interaction strength between O_2 and the inner pore walls of the MOFs. **Co(BPZ)**

affords the highest value of 17.7 kJ/mol calculated at zero coverage, while the Q_{st} trend follows the order **Co(BPZ) > Co(BPZNH$_2$) > Co(BPZNO$_2$)**. The Q_{st} values found for these MOFs are higher than those found for the Co(II) MOFs MFU-1 (11.1 kJ/mol) and MFU-2 (8.5 kJ/mol), built with the 1,4-bis[(3,5-dimethyl)pyrazol-4-yl]benzene ligand and having much higher BET areas (1525 and 1474 m^2/g, respectively).[36] The thermodynamic affinity for O_2 of **Co(BPZ)** is comparable to PCN-9 (17.8 kJ/mol), a Co(II) MOF containing the triazine-2,4,6-triyltribenzoate spacer and with a BET area of 1064 m^2/g.[37]

3.5. Oxidation of cumene over Co(BPZX)

The effect of different ligand tags on the catalytic oxidation of cumene and product distribution was evaluated. The results obtained with **Co(BPZ)** are shown in Table 2 - Entries #2 and #2a, while the whole time-conversion plot is presented in Figure S10 of the Supporting Information. This MOF showed a good catalytic activity for CM oxidation (34% conversion after 7 h) as compared with the blank (autocatalyzed) process (5% conversion under the same reaction conditions, Entry #1). Moreover, **Co(BPZ)** afforded a very high selectivity to CHP: up to ~90% at 8% conversion after 1 h, which is only slightly lower than the autocatalytic process (94%). This selectivity decreased slightly for longer reaction times, down to 84% at 34% conversion after 7 h, along with the formation of PP and AP byproducts. These side products come from the decomposition of CHP, which is catalyzed by the same active sites (Co^{2+} ions) that are involved in CM oxidation.

Table 2. Aerobic oxidation of cumene. Reaction conditions: 1 mL (7.14 mmol) of cumene, catalyst (cumene-to-metal molar ratio = 150), p_{O2} = 4 bar, T = 363 K.

Entry (#)	Catalyst	Time (h)	Conv.(%) [a]	Selectivity (%)			
				CHP	PP	AP	CMD
1	Blank	7	5	94	6	0	0
2	**Co(BPZ)**	1	8	90	10	0	0
2a		7	34	84	15	1	0
3	**Co(BPZNO$_2$)**	1	10	74	22	3	1
3a		7	32	74	22	3	1
4	**Co(BPZNH$_2$)**	1	39	18	71	8	3
4a		7	72	16	69	11	4
4b		24	84	7	73	14	6
5	$Co_3(BTC)_2$ [18,b]	7	49	69	30	1	0
6	Co-salen-polymer [7,c]	12	59	37	57	-	-
7	Co_3O_4 [10,d]	-	-	60	40	-	-

[a] Conversion (mol %), determined by GC. [b] BTC^{3-} = benzene-1,3,5-tricarboxylate. [c] Conditions: p_{O2} = 1 bar; T = 383 K. [d] Conditions: p_{O2} = 1 bar; T = 353 K.

We have recently reported on the catalytic activity of mono- and bimetallic trimesate (benzene-1,3,5-tricarboxylate, BTC^{3-}) compounds prepared from aqueous solutions and employed in the aerobic oxidation of CM.[18] In particular, as compared with $Co_3(BTC)_2$ (Table 2, Entry #5), a lower activity was found for **Co(BPZ)** under the same experimental conditions (34% *vs.* 49% conversion after 7 h, respectively), though the CHP selectivity to was significantly higher: 84% *vs.* 69%, respectively (Entries #2a and #5 in Table 2). These differences in catalysts performance mirror the different chemical properties and coordination environment of the Co^{2+} sites imposed by the ligand nature and the crystal structure.

The introduction of $-NO_2$ groups on the bipyrazolate skeleton has no significant influence on the catalytic activity (Table 2, Entries #3 and #3a): a slightly higher activity was found for **Co(BPZNO$_2$)** at short reaction times as compared to **Co(BPZ)** (10% *vs.* 8% conversion after 1 h, respectively), but both compounds have practically the same activity at longer reaction times, (32% *vs.* 34% conversion after 7 h, respectively). However, small changes were observed in product distribution: a lower CHP selectivity (74%) and a higher formation of PP and AP (Table 2, Entries #3 and #3a) were observed for **Co(BPZNO$_2$)**. Small traces (*ca.* 1%) of an additional heavier product (CMD in Table 2) was also observed, identified as a cumene dimer coming from the direct coupling of two cumyl radicals (Scheme 1).[38]

More important changes are found when $-NH_2$ groups were introduced into the bipyrazolate linker (Table 2, Entries #4 and #4b). In this case, dramatic changes of catalyst activity and cumene oxidation products distribution were observed (see Figure S10 in the Supporting Information): 39% conversion of CM was reached with **Co(BPZNH$_2$) a**fter only 1 h. After 7 h, conversion increased to 72%, while the selectivity to CHP dropped to 16%. Interestingly, the resulting selectivity to PP formation obtained over **Co(BPZNH$_2$)** increased up to 69%. Longer reaction times only produced a slight increase of conversion and selectivity to PP (up to 84% CM conversion and 73% PP selectivity after 24 h), but the amount of CMD increased significantly (6%) as well. The catalytic performance of **Co(BPZNH$_2$)** is better than that observed under similar experimental conditions for the Co-Na heterodinuclear polymer complex based on a Salen Schiff base and a crown ether reported by Wang *et al.* in 2006,[7] in terms of both conversion (72% after 7 h *vs.* 59% after 12 h, entries #4a and #6 in Table 2) and PP selectivity (69% *vs.* 57%). Our catalyst is also better-performing than the classical Co^{2+}/Co^{3+} mixed-oxide Co_3O_4[10] that shows only 40% selectivity for PP (Entry #7 in Table 2).

As mentioned in the Introduction, CHP is the primary product of CM oxidation, while PP and AP come from CHP decomposition. Therefore, PP and AP formation depends on the ability of the Co^{2+} sites to decompose the CHP formed in the main reaction. In line with this observation, for other

MOFs[16, 18] we have observed that an increase of CHP decomposition rate translates into a faster CM conversion and a lower CHP selectivity. Therefore, the differences in product distribution observed in Table 2 for the **Co(BPZX)** MOFs reflects the ability of the catalyst to oxidize CM to CHP and to decompose the formed CHP. To address this point, we designed additional experiments of CHP decomposition over the **Co(BPZX)** samples. The results obtained are summarized in Table 3.

Table 3. Decomposition of CHP over the **Co(BPZX)** MOFs. Reaction conditions: 1 mL of cumene, *ca*. 14 mg of catalyst (CM to Co^{2+} molar ratio = 150), 110 µL of CHP, diphenylether as internal standard (50 µL), N_2 atmosphere, 363 K.

Entry (#)	Catalyst	CHP decomposition[a] (%)	
		at 7 h	at 24 h
1	Blank	2.8	4.4
2	**Co(BPZ)**	4.4	7.1
3	**Co(BPZNO$_2$)**	11.5	17.2
4	**Co(BPZNH$_2$)**	26.6	55.3

[a] CHP decomposition (%) determined by GC.

From a comparison of the data shown in Tables 2 and 3, it is evident that the final CHP selectivity attained in the aerobic oxidation of CM decreases as the ability of the catalyst to decompose CHP increases. Thus, CHP decomposition over **Co(BPZ)** was only slightly faster than in the blank experiment (thermal CHP decomposition, Table 3, Entries #1 and #2): 7.1% *vs.* 4.4% decomposition after 24 h, respectively. Conversely, the decomposition of CHP was much faster over **Co(BPZNH$_2$)**,

attaining 55.3% decomposition after 24 h (Table 3, Entry #4). Meanwhile, the activity of **Co(BPZNO$_2$)** for CHP decomposition lays in between the other two MOFs, as does the final CHP selectivity (Table 3, Entry #3). **Co(BPZNO$_2$)** is slightly more active than **Co(BPZ)** at short reaction times (< 1 h), but it also deactivates faster, due to the formation of the bulky cumene dimers.

It has been reported[39] that the presence of O_2 during CM oxidation can minimize CHP decomposition pathways, thus increasing the final selectivity to CHP. Therefore, the higher affinity of **Co(BPZ)** for O_2 as compared with **Co(BPZNO$_2$)** and **Co(BPZNH$_2$)** according to the estimated isosteric heat of adsorption (Q_{st}, Table 1) might also contribute to some extent to the higher selectivity to CHP observed for **Co(BPZ)**.

In summary, the activity of the scrutinized MOFs for CM conversion and CHP decomposition follows the trend **Co(BPZNH$_2$) >> Co(BPZNO$_2$) > Co(BPZ)**, which is also the opposite trend observed for the CHP selectivity. Therefore, the presence of amino (and, to a minor extent, nitro) groups in the MOF linkers determines the catalytic properties of the solids, inducing a clear *tag-dependent selectivity*. In particular, the amino groups in the 4,4'-bipyrazolate ligand can play a dual role: a local change of the electronic density on Co^{2+} and the introduction of additional adsorption sites for CHP (through hydrogen bonds between CHP and the solid catalyst) that may accelerate CHP decomposition. Although the former effect cannot be ruled out, we think that the latter may have a higher impact on the catalytic properties of the scrutinized MOFs. In this sense, Liao *et al.* have used carbon nanotubes (CNTs) and nitrogen-doped carbon nanotubes (NCNTs) as catalysts for the aerobic oxidation of CM.[40] NCNTs were significantly more active than CNTs for this reaction (74% *vs.* 16% conversion), yielding PP as the main product (96.7% selectivity), while CNTs were highly selective towards CHP (90%). Based on DFT calculations, the authors concluded that the high catalytic activity and PP selectivity of NCNTs is due to a strong interaction with CHP. Thus, once CHP is formed, it remains strongly adsorbed onto the catalyst surface, where it is easily over-oxidized and decomposes to PP. Conversely, the calculated interaction energy between CHP and undoped CNTs was much

lower, so desorption of CHP is more likely to occur. This minimizes CHP decomposition events, thus increasing the final CHP selectivity.

To determine whether the amino groups in **Co(BPZNH$_2$)** play a similar role in determining the catalytic properties for CM oxidation, we have evaluated the strength of the interaction between the catalyst and CM or CHP by measuring their heat of immersion. This technique provides information related to the surface area available to the liquid and, more importantly, to the specific interaction between the solid surface and the wetting liquid.[41] The enthalpy of immersion (ΔH_{imm}) is the enthalpy change at constant temperature arising when a solid is immersed into a wetting liquid in which it does not dissolve nor react.[42] Moreover, immersion in the pure liquid can closely mimic the catalytic conditions used in this work. The results of the heat of immersion experiments are collected in Table 4.

Table 4. Heat of adsorption for selected MOFs in CM and CHP.

	ΔH_{imm} in CM		**ΔH_{imm} in CHP**	
	J/g	**J/m^2**	**J/g**	**J/m^2**
Co(BPZ)	-81	-0.09	-137	-0.15
Co(BPZNH$_2$)	-219	-0.69	-283	-0.89

The heat of immersion in CHP is clearly much higher in the case of **Co(BPZNH$_2$)** than for **Co(BPZ)**: 283 *vs.* 137 J/g, respectively. This difference is still higher if the specific surface area of each compound is taken into account (0.89 *vs.* 0.15 J/m^2, respectively). This is possibly due to the existence of the amino groups in the linkers as additional (stronger) adsorption sites for CHP, reasonably through N–H···O hydrogen bonding interactions between the –NH$_2$ group of BPZNH$_2$ and the –OOH moiety of CHP. Moreover, the heat of immersion in CHP is higher than that in CM for

both **Co(BPZ)** and **Co(BPZNH$_2$)**. This suggests that both MOFs tend to decompose CHP, as already demonstrated in the CHP decomposition experiments summarized in Table 3.

Finally, it is worth mentioning that all the **Co(BPZX)** compounds are stable under the adopted reaction conditions, according to the PXRD patterns recorded after the catalysis. Additional SEM and XPS comparative characterization of **Co(BPZNH$_2$)** before and after catalysis has been carried out, to check for structural or morphological changes occurring to the MOF during the catalytic process. Both SEM images (Figure 5) and the Co 2p and N 1s XPS spectra (Figure 6) of fresh and used **Co(BPZNH$_2$)** have confirmed its stability under the oxidative catalytic conditions used. The Co 2p XPS spectra can be fitted with only one main component with related satellite peaks at BEs ≈ 781 and 796 eV (Figure 6b-c). These peaks are typical of Co^{2+} ions for their $2p_{3/2}$ and $2p_{1/2}$ electronic states, respectively.[43] No Co^{3+} ions are detected, normally associated to bands at lower BEs ≈ 767 ($2p_{3/2}$) and 769 ($2p_{1/2}$) eV.[44] The N 1s XPS spectra can be fitted with one main component and a minor shoulder in a roughly 4:1 ratio at BEs between 399 and 400 eV (Figure 6d-e). While the former component at lower BE can be unambiguously ascribed to N-pyrazole atoms from the linker,[45] peaks centered at 400 eV are likely due to the –NH_2 tag.[46] The curve fitting has ruled out the presence of oxidized functional groups like –NO_2 [whose N(1s) peak is normally centered around 404 eV].[44]

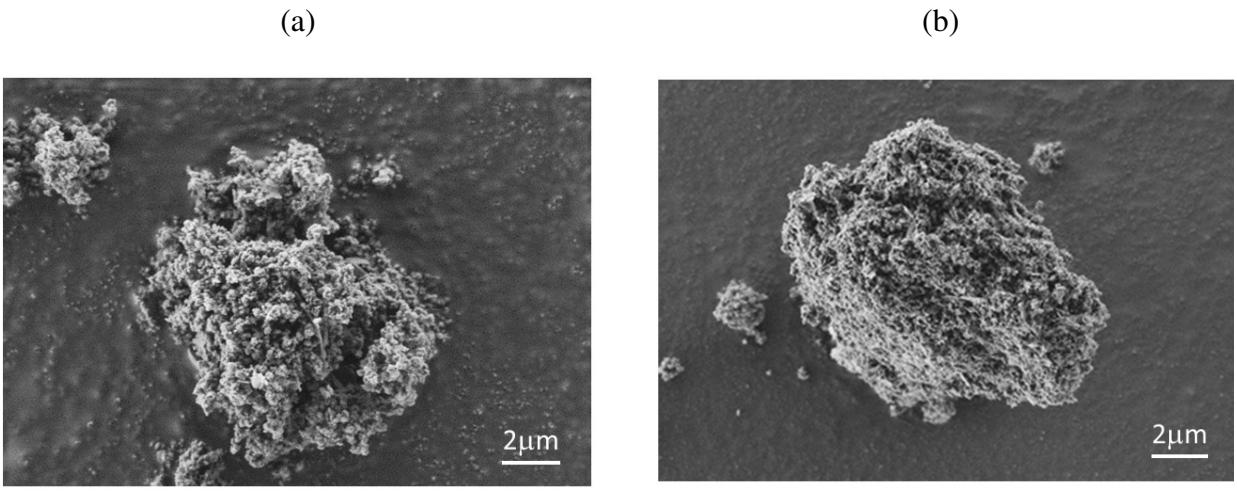

Figure 5. SEM images of fresh (a) and used (b) **Co(BPZNH$_2$)**. No morphological differences can be noticed between the two samples.

(a)

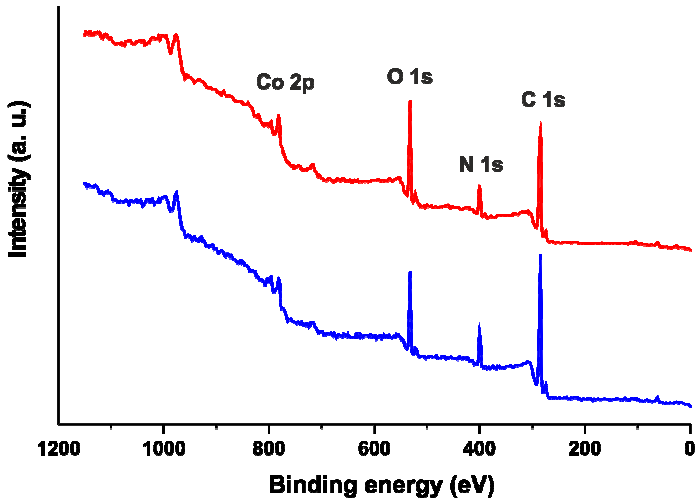
Co 2p
O 1s
C 1s
N 1s
Intensity (a. u.)
1200
1000
800
600
400
200
0
Binding energy (eV)

(b)

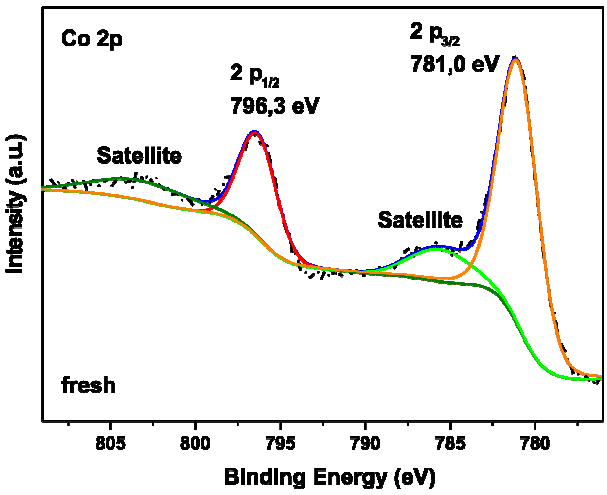
Co 2p
2 p1/2
796,3 eV
2 p3/2
781,0 eV
Satellite
Satellite
fresh
Intensity (a.u.)
805
800
795
790
785
780
Binding Energy (eV)

(c)

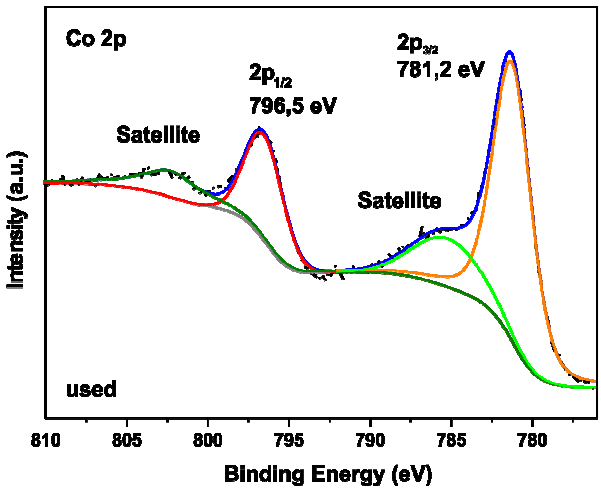
Co 2p
2p1/2
796,5 eV
2p3/2
781,2 eV
Satellite
Satellite
used
Intensity (a.u.)
810
805
800
795
790
785
780
Binding Energy (eV)

(d)

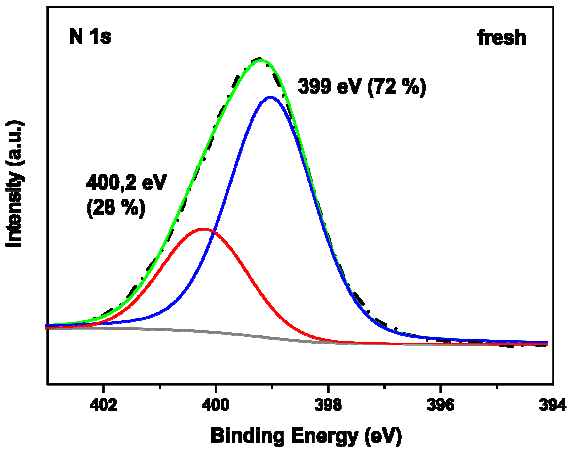
N 1s
fresh
399 eV (72 %)
400,2 eV
(28 %)
Intensity (a.u.)
402
400
398
396
394
Binding Energy (eV)

(e)

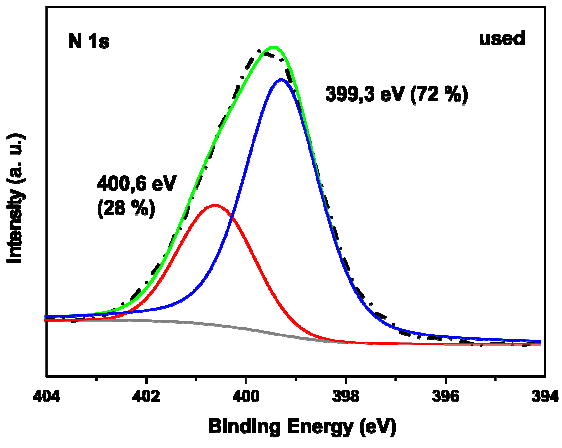
N 1s
used
399,3 eV (72 %)
400,6 eV
(28 %)
Intensity (a. u.)
404
402
400
398
396
394
Binding Energy (eV)

Figure 6. (a) XPS survey spectra recorded for fresh (blue curve) and used (red curve) **Co(BPZNH$_2$)**. XPS Co 2p (b-c) and N 1s (d-e) core level regions of fresh and used **Co(BPZNH$_2$)** along with their relative curve fittings.

Analysis of the filtrates after the reaction by ICP-OES revealed that the amount of Co^{2+} ions leached from the solid catalysts was almost negligible, in all cases below 2% of the total amount of Co^{2+} used in the reaction. Moreover, the MOFs maintained their catalytic activity and CHP (or PP) selectivity practically unmodified for at least five consecutive cycles (see Figure S11).

4. CONCLUSIONS

A series of Co(II) MOFs containing 4,4'-bipyrazolate linkers with different chemical tags has been exploited as heterogeneous catalysts in cumene oxidation. The obtained results have shown that simple ligand functionalization is a good solution to tune the reaction outcome towards the desired product (*tag-dependent selectivity*). Among the tested 4,4'-bipyrazolate materials, **Co(BPZ)** presents good catalytic activity and the best selectivity to CHP, while **Co(BPZNH$_2$)** is featured by high activity. More importantly, **Co(BPZNH$_2$)** turned out to be a good candidate for PP production as the main product. This mirrors the results obtained in CHP decomposition tests and heat of immersion measurements carried out on the scrutinized catalysts. The O_2 affinity of the materials has been quantified through the evaluation of the O_2 isosteric heat of adsorption (Q_{st}), with the trend **Co(BPZ) > Co(BPZNH$_2$) > Co(BPZNO$_2$)**. To the best of our knowledge, this is the first example of the employment of pyrazolate MOFs as catalysts for cumene oxidation and the first case of tag-dependent selectivity ever observed in a MOF. A detailed computational analysis of the reaction mechanism and of the tag-dependent selectivity will be carried out soon, also including other types of chemical tags on the bipyrazolate linker not considered here. The *in silico* screening of the best-performing bipyrazolate MOF for this reaction allows to focus our future experimental synthetic

efforts. Consequently, other *3d* metal-based MOFs containing pyrazolate spacers will be prepared and tested in cumene oxidation, in search for better-performing heterogeneous catalysts for this important industrial reaction.

ASSOCIATED CONTENT

Supporting Information. IR spectrum of **Co(BPZNH$_2$)·DMF**. Graphical results of the whole powder pattern refinements for **Co(BPZNH$_2$)·DMF** under the assumption of the existence of a monophasic or biphasic sample. Graphical result of the final stage of the Rietveld refinement for **Co(BPZNH$_2$)**. TGA and DSC traces of **Co(BPZNH$_2$)·DMF**. VT-PXRD patterns of **Co(BPZNH$_2$)·DMF**. O_2 adsorption isotherms measured on **Co(BPZX)** at 273 K. Time-conversion plots for cumene oxidation with the three MOF catalysts *vs*. blank test. Results of the reusability tests of **Co(BPZ)** and **Co(BPZNH$_2$)** in five consecutive catalytic cycles.

AUTHOR INFORMATION

Corresponding Authors

* Prof. Simona Galli. E-mail: simona.galli@uninsubria.it

* Dr. Andrea Rossin. E-mail: a.rossin@iccom.cnr.it

* Dr. Francesc Llabrés i Xamena. E-mail: fllabres@itq.upv.es

ORCID

Andrea Rossin: 0000-0002-1283-2803

Simona Galli: 0000-0003-0335-5707

Giuliano Giambastiani: 0000-0002-0315-3286

Claudio Pettinari: 0000-0002-2547-7206

Corrado Di Nicola: 0000-0002-0958-6103

Rebecca Vismara: 0000-0001-9474-7671

Marco Moroni: 0000-0001-6167-3792

Francesc Llabrés i Xamena: 0000-0002-4238-5784

Conflicts of Interest. The authors have no conflicts of interest to declare.

ACKNOWLEDGEMENTS

S.G., R.V. and M.M. acknowledge Università dell'Insubria for partial funding. G.G. thanks the Italian MIUR through the PRIN 2017 Project Multi-e: Multielectron Transfer for the Conversion of Small Molecules: an Enabling Technology for the Chemical Use of Renewable Energy (20179337R7) for financial support. G.G. thanks the TRAINER project (Catalysts for Transition to Renewable Energy Future) Ref. ANR-17-MPGA-0017 for support. C.P. thanks the University of Camerino and the Italian MIUR throughout the PRIN 2015 Project Towards a Sustainable Chemistry (20154X9ATP_002). This project has also received funding from the European Union's Horizon 2020 research and innovation program under the Marie Sklodowska-Curie grant agreement No. 641887 (project acronym: DEFNET) and the Spanish Government through projects MAT2017-82288-C2-1-P and Severo Ochoa (SEV-2016-0683). Professor Norberto Masciocchi (University of Insubria, Como, Italy) is acknowledged for fruitful discussions. The authors are also grateful to Dr. Giulia Tuci (CNR-ICCOM Florence, Italy) for help with the XPS curve fitting. The Microscopy Service of the Universitat Politècnica de València is gratefully acknowledged for the electron microscopy measurements.

REFERENCES

1. Fortuin, J. P.; Waterman, H. I., Production of Phenol from Cumene. *Chem. Eng. Sci.* **1953,** *2*, 182-192.
2. (a) Luyben, W. L., Design and Control of the Cumene Process. *Ind. Eng. Chem. Res.* **2010,** *49*, 719–734 (b) Matsui, S.; Fujita, T., New Cumene-Oxidation Systems: O_2 Activator Effects and Radical Stabilizer Effects. *Catal. Today* **2001,** *71*, 145-152.
3. (a) Opeida, I. A.; Kytsya, A. R.; Bazylyak, L. I.; Pobigun, O. I., Silver Nanoparticle Catalysis of the Liquid-Phase Radical Chain Oxidation of Cumene by Molecular Oxygen. *Theor. Exp. Chem.* **2017,** *52*, 369–374 (b) Liquid Phase Aerobic Oxidation Catalysis: Industrial Applications and Academic Perspectives. Shannon, S. S.; Paul, L. A., Eds. John Wiley & Sons: 2016 (c) Tsodikov, M. V.; Kugel, V. Y.; Slivinskii, E. V.; Bondarenko, G. N.; Maksimov, Y. V.; Alvarez, M. A.; Hidalgo, M. C.; Navio, J. A., Selectivity and Mechanism of Cumene Liquid-Phase Oxidation in the Presence of Powdered Mixed Iron-Aluminum Oxides\rprepared by Alkoxy Method. *Appl. Catal. A - Gen.* **2000,** *193*, 237-242 (d) Ismail, S. M., Liquid Phase Oxidation of Cumene over Heretogeneous Catalysts. *J. Chem. Soc. Pak.* **1986,** *8*, 43-47.
4. Zhang, M.; Wang, L.; Ji, H.; Wu, B.; Zeng, X., Cumene Liquid Oxidation to Cumene Hydroperoxide over CuO Nanoparticle with Molecular Oxygen under Mild Condition. *J. Nat. Gas Chem.* **2007,** *16*, 393-398.
5. (a) Hsu, Y. F.; Cheng, C. P., Mechanistic Investigation of the Autooxidation of Cumene Catalyzed by Transition Metal Salts Supported on Polymer. *J. Mol. Catal. A Chem.* **1998,** *136*, 1-11 (b) Hsu, Y. F.; Cheng, C. P., Polymer Supported Catalyst for the Effective Autoxidation of Cumene to Cumene Hydroperoxide. *J. Mol. Catal. A Chem.* **1997,** *120*, 109-116 (c) Hsu, Y. F.; Yen, M. H.; Cheng, C. P., Autooxidation of Cumene Catalyzed by Transition Metal Compounds on Polymeric Supports. *J. Mol. Catal. A Chem.* **1996,** *105*, 137-144.

6. Narulkar, D. D.; Srivastava, A. K.; Butcher, R. J.; Ansy, K. M.; Dhuri, S. N., Synthesis and Characterization of N_3Py_2 Ligand-Based Cobalt(II), Nickel(II) and Copper(II) Catalysts for Efficient Conversion of Hydrocarbons to Alcohols. *Inorg. Chim. Acta* **2017,** *467*, 405-414.
7. Wang, R.-M.; Duan, Z.-F.; He, Y.-F.; Lei, Z.-Q., Heterogeneous Catalytic Aerobic Oxidation Behavior of Co–Na Heterodinuclear Polymeric Complex of Salen-Crown Ether. *J. Mol. Cat. A Chem.* **2006,** *260*, 280-287.
8. Rogovin, M.; Neumann, R., Silicate Xerogels Containing Cobalt as Heterogeneous Catalysts for the Side-Chain Oxidation of Alkyl Aromatic Compounds with *tert*-Butyl Hydroperoxide. *J. Mol. Cat. A Chem.* **1999,** *138*, 315-318.
9. Konopińska, A.; Orlińska, B.; Gillner, D., N-Hydroxyphthalimide as a Catalyst of Cumene Oxidation with Hydroperoxide. *Modern Chemistry* **2017,** *5*, 29-34.
10. Varma, G. R.; Graydon, W. F., Heterogeneous Catalytic Oxidation of Cumene (Isopropyl Benzene) in Liquid Phase. *J. Catal.* **1973,** *28*, 236-244.
11. Collom, S. L.; Bloomfield, A. J.; Anastas, P. T., Advancing Sustainable Manufacturing through a Heterogeneous Cobalt Catalyst for Selective C–H Oxidation. *Ind. Eng. Chem. Res.* **2016,** *55*, 3308-3312.
12. Scognamiglio, J.; Jones, L.; Letizia, C. S.; Api, A. M., Fragrance Material Review on 2-Phenyl-2-Propanol. *Food Chem. Toxicol.* **2012,** *50*, S130-S133.
13. (a) Rossin, A.; Tuci, G.; Luconi, L.; Giambastiani, G., Metal–Organic Frameworks as Heterogeneous Catalysts in Hydrogen Production from Lightweight Inorganic Hydrides. *ACS Catal.* **2017,** *7*, 5035–5045 (b) Chughtai, A. H.; Ahmad, N.; Younus, H. A.; Laypkovc, A.; Verpoort, F., Metal–Organic Frameworks: Versatile Heterogeneous Catalysts for Efficient Catalytic Organic Transformations. *Chem. Soc. Rev.* **2015,** *44*, 6804-6849 (c) Liu, J.; Chen, L.; Cui, H.; Zhang, J.; Zhang, L.; Su, C.-Y., Applications of Metal–Organic Frameworks in Heterogeneous Supramolecular Catalysis. *Chem. Soc. Rev.* **2014,** *43*, 6011-6061 (d) Gascon, J.;

Corma, A.; Kapteijn, F.; Llabrés i Xamena, F. X., Metal Organic Framework Catalysis: *Quo Vadis*? *ACS Catal.* **2014,** *4*, 361–378.

14. (a) Luo, S.; Zeng, Z.; Zeng, G.; Liu, Z.; Xiao, R.; Chen, M.; Tang, L.; Tang, W.; Lai, C.; Cheng, M.; Shao, B.; Liang, Q.; Wang, H.; Jiang, D., Metal Organic Frameworks as Robust Host of Palladium Nanoparticles in Heterogeneous Catalysis: Synthesis, Application and Prospect. *ACS Appl. Mater. Interfaces* **2019,** *11*, 32579-32598 (b) Deng, X.; Li, Z.; García, H., Visible Light Induced Organic Transformations Using Metal-Organic-Frameworks (MOFs). *Chem. - Eur. J.* **2017,** *23*, 11189-11209 (c) Dhakshinamoorthy, A.; Asiri, A. M.; García, H., Metal–Organic Frameworks as Catalysts for Oxidation Reactions. *Chem. - Eur. J.* **2016,** *22*, 8012-8024.
15. (a) Song, X.; Hu, D.; Yang, X.; Zhang, H.; Zhang, W.; Li, J.; Jia, M.; Yu, J., Polyoxomolybdic Cobalt Encapsulated within Zr-Based Metal−Organic Frameworks as Efficient Heterogeneous Catalysts for Olefins Epoxidation. *ACS Sustainable Chem. Eng.* **2019,** *7*, 3624-3631 (b) Zhang, T.; Hu, Y.-Q.; Han, T.; Zhai, Y.-Q.; Zheng, Y.-Z., Redox-Active Cobalt(II/III) Metal−Organic Framework for Selective Oxidation of Cyclohexene. *ACS Appl. Mater. Interfaces* **2018,** *10*, 15786-15792 (c) Ma, Y.; Peng, H.; Liu, J.; Wang, Y.; Hao, X.; Feng, X.; Khan, S. U.; Tan, H.; Li, Y., Polyoxometalate-Based Metal−Organic Frameworks for Selective Oxidation of Aryl Alkenes to Aldehydes. *Inorg. Chem.* **2018,** *57*, 4109-4116 (d) Othong, J.; Boonmak, J.; Ha, J.; Leelasubcharoen, S.; Youngme, S., Thermally Induced Single-Crystal-to-Single-Crystal Transformation and Heterogeneous Catalysts for Epoxidation Reaction of Co(II) Based Metal−Organic Frameworks Containing 1,4-Phenylenediacetic Acid. *Cryst. Growth Des.* **2017,** *17*, 1824-1835 (e) Wang, J.-C.; Ding, F.-W.; Ma, J.-P.; Liu, Q.-K.; Cheng, J.-Y.; Dong, Y.-B., Co(II)-MOF: A Highly Efficient Organic Oxidation Catalyst with Open Metal Sites. *Inorg. Chem.* **2015,** *54*, 10865-10872 (f) Tuci, G.; Giambastiani, G.; Kwon, S.; Stair, P. C.; Snurr, R. Q.; Rossin, A., Chiral Co(II) Metal−Organic Framework in the Heterogeneous Catalytic Oxidation of Alkenes under Aerobic and Anaerobic Conditions. *ACS Catal.* **2014,** *4*, 1032-1039 (g) Hamidipour, L.;

Farzaneh, F., Cobalt Metal Organic Framework as an Efficient Heterogeneous Catalyst for the Oxidation of Alkanes and Alkenes. *Reac. Kinet. Mech. Cat.* **2013,** *109*, 67-75.

16. Luz, I.; Leon, A.; Boronat, M.; Llabrés i Xamena, F. X.; Corma, A., Selective Aerobic Oxidation of Activated Alkanes with MOFs and their Use for Epoxidation of Olefins with Oxygen in a Tandem Reaction. *Cat. Sci. Technol.* **2013,** *3*, 371-379.
17. Santiago-Portillo, A.; Navalon, S.; Cirujano, F. G.; Llabrés i Xamena, F. X.; Alvaro, M.; Garcia, H., MIL-101 as Reusable Solid Catalyst for Autoxidation of Benzylic Hydrocarbons in the Absence of Additional Oxidizing Reagents. *ACS Catal.* **2015,** *5*, 3216.
18. Nowacka, A.; Briantais, P.; Prestipino, C.; Llabrés i Xamena, F. X., Selective Aerobic Oxidation of Cumene to Cumene Hydroperoxide over Mono- and Bimetallic Trimesate Metal–Organic Frameworks Prepared by a Facile "Green" Aqueous Synthesis. *ACS Sustainable Chem. Eng.* **2019,** *7*, 7708–7715.
19. (a) Vismara, R.; Tuci, G.; Tombesi, A.; Domasevitch, K. V.; Di Nicola, C.; Giambastiani, G.; Chierotti, M. R.; Bordignon, S.; Gobetto, R.; Pettinari, C.; Rossin, A.; Galli, S., Tuning Carbon Dioxide Adsorption Affinity of Zinc(II) MOFs by Mixing Bis(pyrazolate) Ligands with N□Containing Tags. *ACS Appl. Mater. Interfaces* **2019,** *11*, 26956-26969 (b) Vismara, R.; Tuci, G.; Mosca, N.; Domasevitch, K. V.; Di Nicola, C.; Pettinari, C.; Giambastiani, G.; Galli, S.; Rossin, A., Amino-Decorated Bis(Pyrazolate) Metal-Organic Frameworks for Carbon Dioxide Capture and Green Conversion into Cyclic Carbonates. *Inorg. Chem. Front.* **2019,** *6*, 533-545 (c) Mosca, N.; Vismara, R.; Fernandes, J. A.; Tuci, G.; Di Nicola, C.; Domasevitch, K. V.; Giacobbe, C.; Giambastiani, G.; Pettinari, C.; Aragones-Anglada, M.; Moghadam, P. Z.; Fairen-Jimenez, D.; Rossin, A.; Galli, S., Nitro-Functionalized Bis(Pyrazolate) Metal-Organic Frameworks as Carbon Dioxide Capture Materials under Ambient Conditions. *Chem.-Eur. J.* **2018,** *24*, 13170-13180 (d) Petti□ari, C.; Tăbăcaru, A.; Galli, S., Coordi□atio□ Polymers a□d Metal–Organic Frameworks Based on Poly(Pyrazole)-Containing Ligands. *Coord. Chem. Rev.* **2016,** *307*, 1-31 (e) Pettinari, C.; Tăbăcaru, A.; Boldog, I.; Domasevitch, K. V.; Galli, S.; Masciocchi, N., Novel Coordination

Frameworks Incorporating the 4,4′-Bipyrazolyl Ditopic Ligand. *Inorg. Chem.* **2012,** *51*, 5235–5245 (f) Colombo, V.; Montoro, C.; Maspero, A.; Palmisano, G.; Masciocchi, N.; Galli, S.; Barea, E.; Navarro, J. A. R., Tuning the Adsorption Properties of Isoreticular Pyrazolate-Based Metal–Organic Frameworks through Ligand Modification. *J Am. Chem. Soc.* **2012,** *134*, 12830-12843 (g) Tăbăcaru, A.; Petti□ari, C.; Masciocchi, N.; Galli, S.; Marchetti, F.; A□gjellari, M., Pro-porous Coordination Polymers of the 1,4-Bis((3,5-dimethyl-1H-pyrazol-4-yl)-methyl)benzene Ligand with Late Transition Metals. *Inorg. Chem.* **2011,** *50*, 11506-11513 (h) Colombo, V.; Galli, S.; Choi, H. J.; Han, G. D.; Maspero, A.; Palmisano, G.; Masciocchi, N.; Long, J. R., High Thermal and Chemical Stability in Pyrazolate-Bridged Metal–Organic Frameworks with Exposed Metal Sites. *Chem. Sci.* **2011,** *2*, 1311-1319 (i) Masciocchi, N.; Galli, S.; Colombo, V.; Maspero, A.; Palmisano, G.; Seyyedi, B.; Lamberti, C.; Bordiga, S., Cubic Octanuclear Ni(II) Clusters in Highly Porous Polypyrazolyl-Based Materials. *J. Am. Chem. Soc.* **2010,** *132*, 7902–7904 (j) Galli, S.; Masciocchi, N.; Colombo, V.; Maspero, A.; Palmisa□o, G.; López-Garzó□, F. J.; Domi□go-García, M.; Fer□á□dez-Morales, I.; Barea, E.; Navarro, J. A. R., Adsorption of Harmful Organic Vapors by Flexible Hydrophobic Bis-pyrazolate Based MOFs. *Chem. Mater.* **2010,** *22*, 1664−1672.

20. Boldog, I.; Sieler, J.; Chernega, A. N.; Domasevitch, K. V., 4,4′-Bipyrazolyl: New Bitopic Connector for Construction of Coordination Networks. *Inorg. Chim. Acta* **2002,** *338*, 69-77.
21. Domasevitch, K. V.; Gospodinov, I.; Krautscheid, H.; Klapötke, T. M.; Stierstorfer, J., Facile and Selective Polynitrations at the 4-Pyrazolyl Dual Backbone: Straightforward Access to a Series of High-Density Energetic Materials. *New J. Chem.* **2019,** *43*, 1305-1312.
22. TOPAS-Academic 6, Bruker, by Coelho Software, Brisbane, Australia **2016**.
23. Coelho, A. A., Indexing of Powder Diffraction Patterns by Iterative Use of Singular Value Decomposition. *J . Appl. Crystallogr.* **2003,** *36*, 86-95.
24. (a) Cheetham, A. K.; Bennett, T. D.; Coudert, F.-X.; Goodwin, A. L., Defects and Disorder in Metal Organic Frameworks. *Dalton Trans.* **2016,** *45*, 4113-4126 (b) Cliffe, M. J.; Wan, W.; Zou, X.; Chater, P. A.; Kleppe, A. K.; Tucker, M. G.; Wilhelm, H.; Funnell, N. P.; Coudert, F.-X.;

Goodwin, A. L., Correlated Defect Nanoregions in a Metal–Organic Framework. *Nature Commun.* **2014,** *5*, 4176.

25. (a) Spirkl, S.; Grzywa, M.; Volkmer, D., Synthesis and Characterization of a Flexible Metal Organic Framework Generated from Mn^{III} and the 4,4'-Bipyrazolate-Ligand. *Dalton Trans.* **2018,** *47*, 8779–8786 (b) Nazarenko, O. M.; Rusanov, B.; Chernega, A. N.; Domasevitch, K. V., Cobalt(II) and Cadmium(II) Square Grids Supported with 4,4'-Bipyrazole and Accommodating 3-Carboxyadamantane-1-Carboxylate. *Acta Cryst.* **2013,** *C69*, 232-236 (c) Tăbăcaru, A.; Pettinari, C.; Marchetti, F.; Di Nicola, C.; Domasevitch, K. V.; Galli, S.; Masciocchi, N.; Scuri, S.; Grappasonni, I.; Cocchioni, M., Antibacterial Action of 4,4′-Bipyrazolyl-Based Silver(I) Coordination Polymers Embedded in PE Disks. *Inorg. Chem.* **2012,** *51*, 9775-9788 (d) Sun, Q.-F.; Wong, K. M.-C.; Liu, L.-X.; Huang, H.-P.; Yu, S.-Y.; Yam, V. W.-W.; Li, Y.-Z.; Pan, Y.-J.; Yu, K.-C., Self-Assembly, Structures, and Photophysical Properties of 4,4′-Bipyrazolate-Linked Metallo-Macrocycles with Dimetal Clips. *Inorg. Chem.* **2008,** *47*, 2142-2154 (e) Lozan, V.; Solntsev, P. Y.; Leibeling, G.; Domasevitch, K. V.; Kersting, B., Tetranuclear Nickel Complexes Composed of Pairs of Dinuclear LNi_2 Fragments Linked by 4,4′□Bipyrazolyl, 1,4□Bis(4′□ pyrazolyl)benzene, and 4,4′□Bipyridazine: Synthesis, Structures, and Magnetic Properties. *Eur. J. Inorg. Chem.* **2007**, 3217-3226.

26. Bond distances and angles for the rigid body describing the ligand: C-C and C-N of the pyrazole ring 1.36 Å; exocyclic C-C 1.40 Å; C-H of the pyrazole ring 0.95 Å; $C\text{-}N_{NH2}$ 1.40 Å; N-H 0.95 Å; pyrazole ring internal and external bond angles 108° and 126°, respectively; angles at the nitrogen atom of the amino group 120°.

27. Coelho, A. A., Whole-Profile Structure Solution from Powder Diffraction Data Using Simulated Annealing. *J. Appl. Crystallogr.* **2000,** *33*, 899-908.

28. Cheary, R. W.; Coelho, A. A., A Fundamental Parameters Approach to X-Ray Line-Profile Fitting. *J. Appl. Cryst.* **1992,** *25*, 109-121.

29. Stephens, P. W., Phenomenological Model of Anisotropic Peak Broadening in Powder Diffraction. *J . Appl. Crystallogr.* **1999,** *32*, 281-289.

30. Rouquerol, J.; Llewellyn, P.; Rouquerol, F., In *Studies in Surface Science and Catalysis*, Llewellyn, P. L.; Rodriquez-Reinoso, F.; Rouquerol, J.; Seaton, N., Eds. Elsevier Amsterdam, 2007; Vol. 160, p 49.

31. Saeidi, N.; Parvin, M., Accuracy of Dubinin-Astakhov and Dubinin-Radushkevich Adsorption Isotherm Models in Evaluating Micropore Volume of Bentonite. *Periodica Polytech., Chem. Eng.* **2016,** *60*, 123-129.

32. (a) Zhu, X.; Tian, C.; Veith, G. M.; Abney, C. W.; Dehaudt, J.; Dai, S., *In Situ* Doping Strategy for the Preparation of Conjugated Triazine Frameworks Displaying Efficient CO_2 Capture Performance. *J. Am. Chem. Soc.* **2016,** *138*, 11497–11500 (b) Zhu, X.; Mahurin, S. M.; An, S.-H.; Do-Thanh, C.-L.; Tian, C.; Li, Y.; Gill, L. W.; Hagaman, E. W.; Bian, Z.; Zhou, J.-H.; Hu, J.; Liu, H.; Dai, S., Efficient CO_2 Capture by a Task-Specific Porous Organic Polymer Bifunctionalized with Carbazole and Triazine Groups. *Chem. Commun.* **2014,** *50*, 7933-7936.

33. The empty volume was estimated with the software PLATON (Spek, A. L. *Acta Crystallogr. Sect. D* **2009**, *65*, 148–155).

34. Blatov, V. A.; Shevchenko, A. P.; Proserpio, D. M., Applied Topological Analysis of Crystal Structures with the Program Package ToposPro. *Cryst. Growth Des.* **2014,** *14*, 3576-3586.

35. Bertier, P.; Schweinar, K.; Stanjek, H.; Ghanizadeh, A.; Clarkson, C. R.; Busch, A.; Kampan, N.; Prinz, D.; Amann-Hildenbrand, A.; Krooss, B. M.; Pipich, V., On the Use and Abuse of N_2 Physisorption for the Characterization of the Pore Structure of Shales *CMS Work. Lect.* **2016,** *21*, 151-161.

36. Tonigold, M.; Lu, Y.; Mavrandonakis, A.; Puls, A.; Staudt, R.; Moellmer, J.; Sauer, J.; Volkmer, D., Pyrazolate-Based Cobalt(II)-Containing Metal–Organic Frameworks in Heterogeneous Catalytic Oxidation Reactions: Elucidating the Role of Entatic States for Biomimetic Oxidation Processes. *Chem. - Eur. J.* **2011,** *17*, 8671-8695.

37. Ma, S.; Zhou, H.-C., A Metal-Organic Framework with Entatic Metal Centers Exhibiting High Gas Adsorption Affinity. *J. Am. Chem. Soc.* **2006,** *128*, 11734-11735.

38. Wang, Z.-J.; Lv, J.-J.; Yi, R.-N.; Xiao, M.; Feng, J.-J.; Liang, Z.-W.; Wang, A.-J.; Xu, X., Nondirecting Group sp^3 C-H Activation for Synthesis of Bibenzyls via Homo-coupling as Catalyzed by Reduced Graphene Oxide Supported PtPd@Pt Porous Nanospheres. *Adv. Synth. Catal.* **2018,** *360*, 932-941.

39. Casemier, J. H. R.; Nieuwenhuys, B. E.; Sachtler, W. M. H., The Oxidation of Cumene and the Decomposition of Cumene Hydroperoxide on Silver, Copper, And Platinum. *J. Catal.* **1973,** *29*, 367-373.

40. Liao, S.; Chi, Y.; Yu, H.; Wang, H.; Peng, F., Tuning the Selectivity in the Aerobic Oxidation of Cumene Catalyzed by Nitrogen-Doped Carbon Nanotubes. *ChemCatChem* **2014,** *6*, 555–560.

41. Silvestre-Albero, J.; Gómez de Salazar, C.; Sepúlveda-Escribano, A.; Rodríguez-Reinoso, F., Characterization of Microporous Solids by Immersion Calorimetry. *Colloid. Surface A* **2001,** *187-188*, 151-165.

42. Everett, D. H., Manual of Symbols and Terminology for Physicochemical Quantities and Units, Appendix II: Definitions, Terminology and Symbols in Colloid and Surface Chemistry. *Pure Appl. Chem.* **1972,** *31*, 579.

43. (a) Liu, C.; Wang, T.; Ji, J.; Wang, C.; Wang, H.; Jin, P.; Zhou, W.; Jiang, J., The Effect of Pore Size and Layer Number of Metal–Porphyrin Coordination Nanosheets on Sensing DNA. *J. Mater. Chem. C* **2019,** *7*, 10240-10246 (b) Gong, T.; Yang, X.; Fang, J.-J.; Sui, Q.; Xi, F.-G.; Gao, E.-Q., Distinct Chromic and Magnetic Properties of Metal–Organic Frameworks with a Redox Ligand. *ACS Appl. Mater. Interfaces* **2017,** *9*, 5503-5512.

44. Wagner, C. D., Eds., *The NIST X-Ray Photoelectron Spectroscopy (XPS) Database*. National Institute of Standards and Technology - USA: 1991.

45. (a) Yamada, Y.; Kim, J.; Matsuo, S.; Sato, S., Nitrogen-Containing Graphene Analyzed by X-Ray Photoelectron Spectroscopy. *Carbon* **2014,** *70*, 59-74 (b) Singhbabu, Y. N.; Kumari, P.;

Parida, S.; Sahu, R. K., Conversion of Pyrazoline to Pyrazole in Hydrazine Treated N-Substituted Reduced Graphene Oxide Films Obtained by Ion Bombardment and their Electrical Properties. *Carbon* **2014,** *74*, 32-43.

46. A.P. Dementjev, A. P.; de Graaf, U. A.; van de Sanden, M. C. M.; Maslakov, K. I.; Naumkin, A. V.; Serov, A. A., X-Ray Photoelectron Spectroscopy Reference Data for Identification of the C_3N_4 Phase in Carbon-Nitrogen Films. *Diam. Relat. Mater.* **2000,** *9*, 1904-1907.

Table of Contents

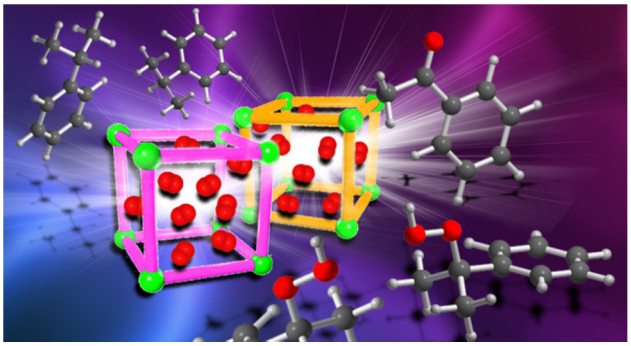

SYNOPSIS. Cumene aerobic oxidation catalysed by Co(II) bipyrazolate MOFs decorated with assorted functional groups is featured by a tag-dependent selectivity. The untagged MOF **Co(BPZ)** shows the best selectivity to cumene hydroperoxide, while the amino-tagged catalyst **Co(BPZNH$_2$)** gives 2-phenyl-2-propanol as preferential oxidation product.